Available online at www.sciencedirect.com
ScienceDirect
European Journal of Mechanics B/Fluids 27 (2008) 219–238

Influence of pitching angle of incidence on the dynamic stall behavior of a symmetric airfoil

Sunetra Sarkar *,[1], Kartik Venkatraman

Department of Aerospace Engineering, Indian Institute of Science, Bangalore, India 560012

Received 1 November 2005; accepted 24 July 2006

Available online 24 May 2007

Abstract

This study presents the influence of pitch angle of an airfoil on its near-field vortex structure as well as the aerodynamic loads during a dynamic stall process. Dynamic stall behavior in a sinusoidally pitching airfoil is usually analyzed at low to medium reduced frequencies and with the maximum angle of attack of the airfoil not exceeding 25°. In this work, we study dynamic stall of a symmetric airfoil at medium to high reduced frequencies even as the maximum angle of attack goes from 25° to 45°. The evolution and growth of the laminar separation bubble, also known as a dynamic stall vortex, at the leading edge and the trailing edge are studied as the pitch cycle goes from the minimum to the maximum angle of attack. The effect of reduced frequencies on the vortex structure as well as the aerodynamic load coefficients is investigated. The reduced frequency is shown to be a bifurcation parameter triggering period doubling behavior. However, the bifurcation pattern is dependent on the variation of the pitch angle of incidence of the airfoil.

Keywords: Discrete vortex technique; Dynamic stall vortex; Period doubling behavior

1. Introduction

Dynamic stall involves a complex dynamical phenomenon associated with a stall delay when an airfoil is subjected to very high angles of attack in some time dependent fashion. The aerodynamic forces increase much beyond their static stall values before finally dropping off at an angle of attack considerably higher than the static stall angle. The airfoil in such condition is said to be in 'deep stall' regime. A leading edge vortex develops during the airfoil's movement towards a high angle of attack which increases the suction and unsteady aerodynamic forces. The growth and behavior of this leading edge vortex influence the flow structure as well as the aerodynamic loading during dynamic stall. Therefore, flow or system parameters which affect the evolution of this leading edge vortex, also called dynamic stall vortex, influence the aerodynamic loads at the dynamic stall regime.

Carr [1] has presented a comprehensive review of the dynamic stall research during the seventies and eighties of the last century. The main focus has been given on discussing the role of various parameters on the dynamic stall

* Corresponding author.
E-mail address: sunetra.sarkar@gmail.com (S. Sarkar).
[1] Present address: Department of Aerospace Engineering, Technical University of Delft, The Netherlands.

0997-7546/$ – see front matter
doi:10.1016/j.euromechflu.2006.07.004

event. Effect of parameters like free stream velocity, pitch axis location have been discussed along with the influence of mean angle, amplitude and frequency. Visbal and Shang [2] have presented a numerical study of an airfoil pitching at constant rates to very high angles of attack. The computational model considers a 2-D compressible ($M = 0.2$) Navier–Stokes model with laminar flow assumptions ($Re = 1 \times 10^4$). A NACA 0015 airfoil has been subjected to large pitching movements at constant rates. Numerical results have been compared with experimental observations. Effects of pitch rate and pitch axis location have been studied in detail. Visbal [3] has extended the previous study [2] and investigated the effect of a wider variety of pitch rates on dynamic stall. A turbulent flow model has been assumed. The effect of the Mach number has also been investigated by varying the free stream Mach number form (0.2–0.6). At higher Mach numbers, the dynamic stall process is controlled by the shock/boundary layer interaction and not by the formation of a leading edge vortex. Tuncer et al. [4] have investigated the unsteady flow fields around airfoils sinusoidally oscillating in pitch and associated dynamic stall phenomenon using a numerical simulation. They have considered a velocity–vorticity formulation of the incompressible Navier–Stokes equations. This consists of a vorticity transport equation and an integral equation for velocity. They have also incorporated a two-layer algebraic turbulence model developed by Baldwin and Lomax. Along with the full viscous analysis, a simplified vortical flow analysis has also been considered for attached flow fields. In the latter, it has been assumed that the viscous flow zone is confined to a thin boundary layer region around the airfoil and to a wake behind it. The pitching oscillation considers an airfoil pitching between (5°–25°), at reduced frequencies $k = \omega c/V_\infty$ = 0.2, 0.3 and 0.5 at a Reynolds number (Re) of 1×10^6. The growth and movement of the leading edge vortex have been studied in details using a full viscous analysis. The numerical observations have been compared with experimental results and a good match has been reported.

The starting flow past a NACA 0012 airfoil translating and oscillating at large angles of attack has been examined by Ohmi et al. [5,6]. They have used flow visualization techniques and numerical calculations. A very wide variation of the angles of attack has been considered. The Reynolds number assumed were 1500, 3000 and 10 000. The reduced frequency, defined as $fc/(2V_\infty)$ (f in Hz) has been taken to be equal to 0.1, 0.5 and 1.0. The effect of the reduced frequency has been found to be most significant. Effect of mean incidence and amplitude has been discussed at different frequencies. The effect of pitch axis location is small at lower reduced frequencies and at the higher values, different types of vortex patterns are seen. The effect of the Reynolds number has been found to be small compared to other parameters.

Carr and Chandrasekhara [7] have presented a comprehensive review on the effect of compressibility on the dynamic stall process, both in aircraft wings and helicopter blades. Two direct effect of compressibility on the dynamic stall process have been listed: appearance of local supersonic flow on the airfoil and increase in drag. As the angle of attack increases, the local velocity around the leading edge of the airfoil increases many times that of the free stream value. As a result, local supersonic flow occurs on the airfoil, even when the free stream Mach number is relatively low. This is a direct effect of compressibility on the dynamic stall process. As the supersonic region increases in strength, shocks may develop, which generates shock induced drags, thus the drag on the airfoil will increase significantly. Effect of Mach number on the dynamic stall process has been presented in details. Ekaterinaris and Platzer [8] have presented a discussion on various computational models in order to predict the wake patterns and aerodynamic loads during dynamic stall. Major numerical approaches used by various researchers over the years, for example, potential flow, boundary layer techniques, viscous-inviscid interaction and Navier–Stokes methods have been described.

Other numerical computations on sinusoidal large amplitude pitching motions also include a recent study by Akbari and Price [9]. They have considered an incompressible Navier–Stokes equation in the vorticity stream function form and introduced a grid in the flow field to solve the Poisson's equation for the stream function with given vorticity, to calculate the velocity field from the stream functions and also to solve the diffusion equation for the vorticity field. A laminar flow model has been assumed at Reynolds number $Re = 1 \times 10^4$. The parameters whose influence on the dynamic stall event have been studied include, reduced frequency of pitching oscillations, Reynolds number, mean angle of attack and pitching axis location. The pitching angles have been varied around a static stall angle of 15° and the reduced frequencies considered are $k = \omega c/V_\infty = 0.3$, 0.5 and 1. Results at these k values have been compared with [4]. Some differences in the load coefficient patterns due to Reynolds number discrepancies have been pointed out. Considering a higher value of the mean incidence, it has been shown that higher hysteresis effects in the load coefficient plots are visible; in general, the maximum value and the average of the load coefficients are greater.

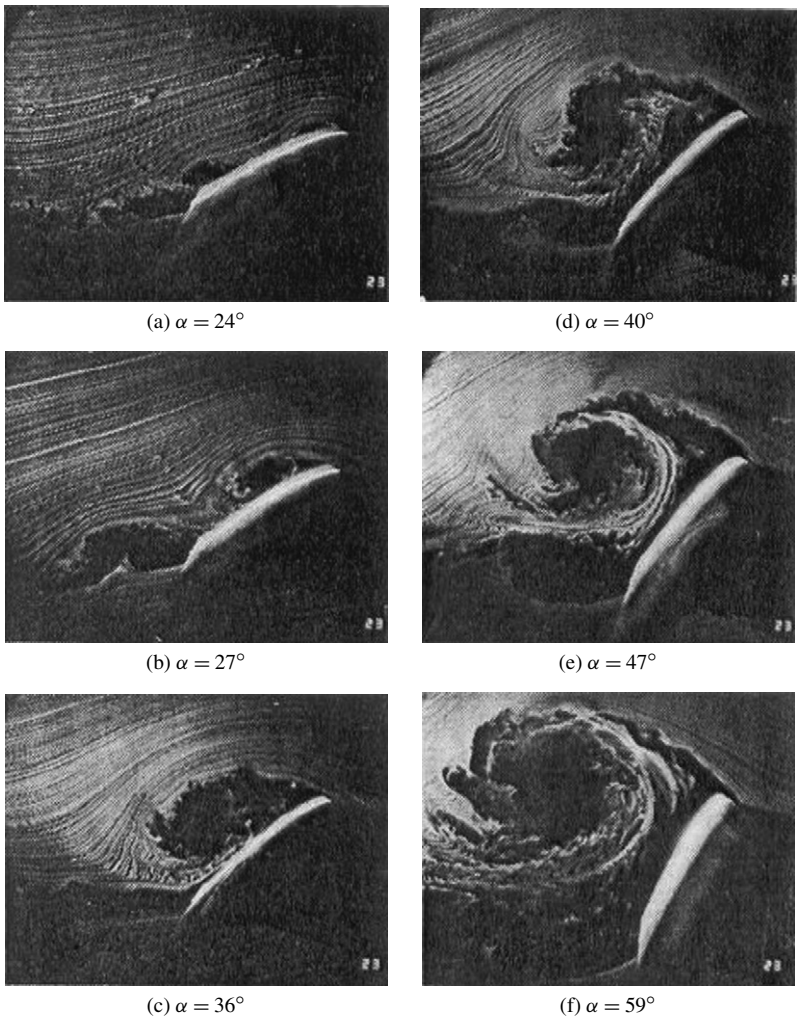

(a) $\alpha = 24°$ (d) $\alpha = 40°$

(b) $\alpha = 27°$ (e) $\alpha = 47°$

(c) $\alpha = 36°$ (f) $\alpha = 59°$

Fig. 1. Experimentally observed evolution of vortex pattern, Walker et al. [22]. $Re = 4.5 \times 10^4$; $\dot{\alpha}c/V_\infty = 0.2$.

Most earlier studies on sinusoidal pitching focus on moderate angles of attack, a maximum around 25° and reduced frequency $k = \omega c/V_\infty$ below 1. However, it is apparent that an increase in the total angle of attack rather than the mean or amplitude of angle of attack, should significantly influence the leading edge vortex growth which in turn will affect the aerodynamic loads [6]. The focus of the present study has been to investigate the growth and evolution of dynamic stall vortex at different reduced frequencies (beyond 1) as the maximum angle of attack changes from 25° to 45°. We have observed a period doubling pattern in the vortex behavior at higher frequency range, which has not been reported before. We compare the vortex patterns at the same reduced frequency values for different maximum angle of attack cases. We also discuss their consequences on the aerodynamic loads. The fluid dynamics in this study has been simulated using a discrete vortex technique [10–12].

2. The random discrete vortex method

An incompressible viscous flow can be described in terms of its vorticity $\vec{\Omega} = \nabla \times \vec{V}$ as [13]

$$\frac{D\vec{\Omega}}{Dt} = \frac{\partial \vec{\Omega}}{\partial t} + \vec{V} \cdot \nabla \vec{\Omega} = \vec{\Omega} \cdot \nabla \vec{V} + \nu \nabla^2 \vec{\Omega}, \tag{1}$$

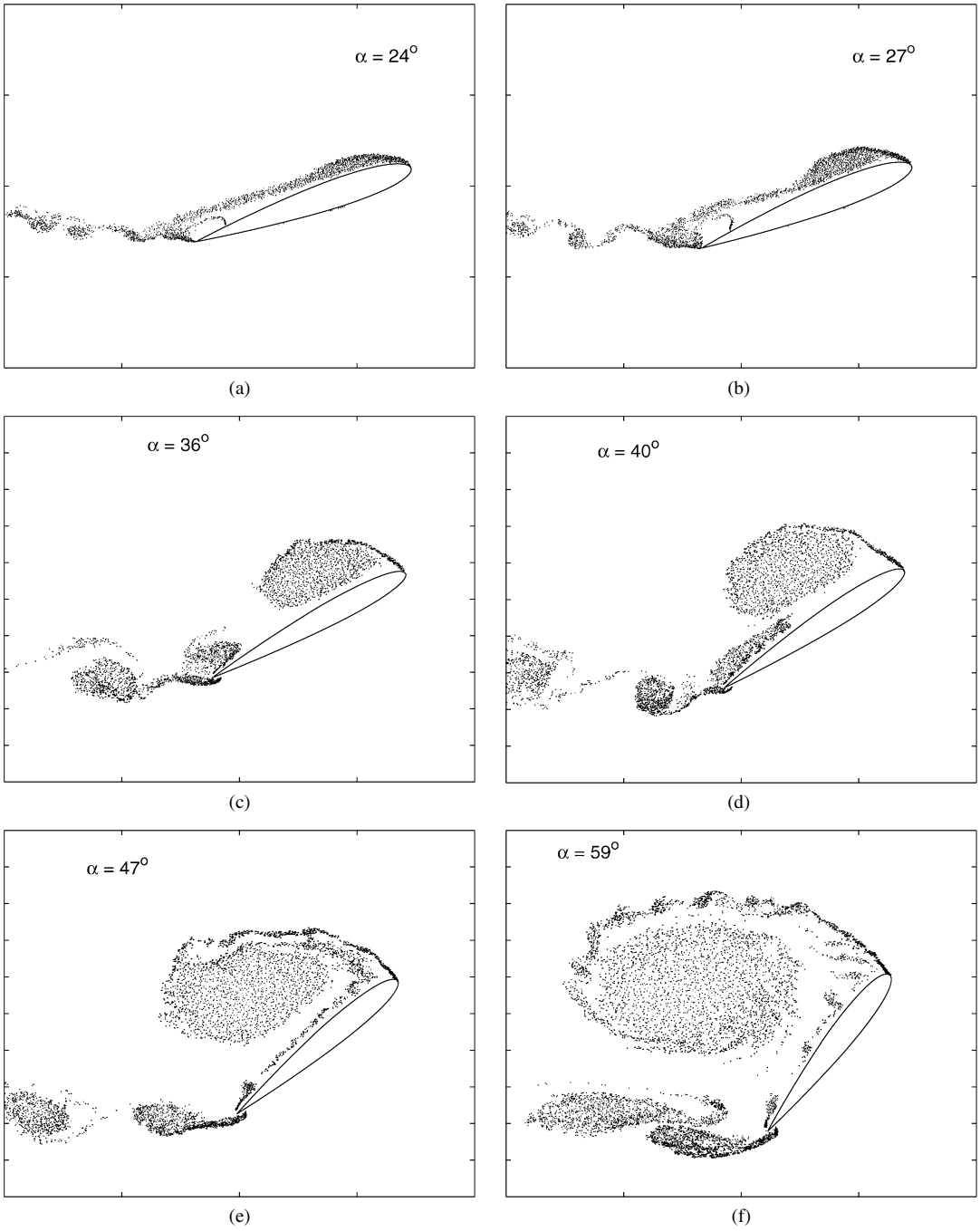

Fig. 2. Unsteady flow past airfoil pitching at constant rate. $\alpha(\dot{t})c/V_\infty = 0.2$; $Re = 4.5 \times 10^4$; $a = -1/4$.

where ν is the viscosity and $\vec{V}$ is the velocity field. The $\vec{\Omega} \cdot \nabla \vec{V}$ term gives the rate of deformation of the vortex lines and exists only in three-dimensional flow. Hence for a 2-D incompressible flow the vorticity transport equation is rewritten in the form

$$\frac{D\Omega}{Dt} = \nu \nabla^2 \Omega. \tag{2}$$

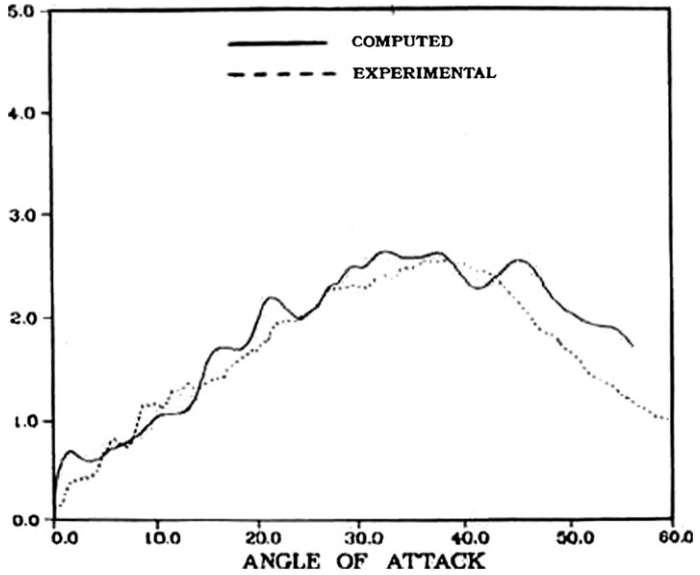

Fig. 3. Experimental verification of lift coefficient from [2], $\dot{\alpha(t)}c/V_\infty = 0.2$; $Re = 4.5 \times 10^4$; $a = -1/4$.

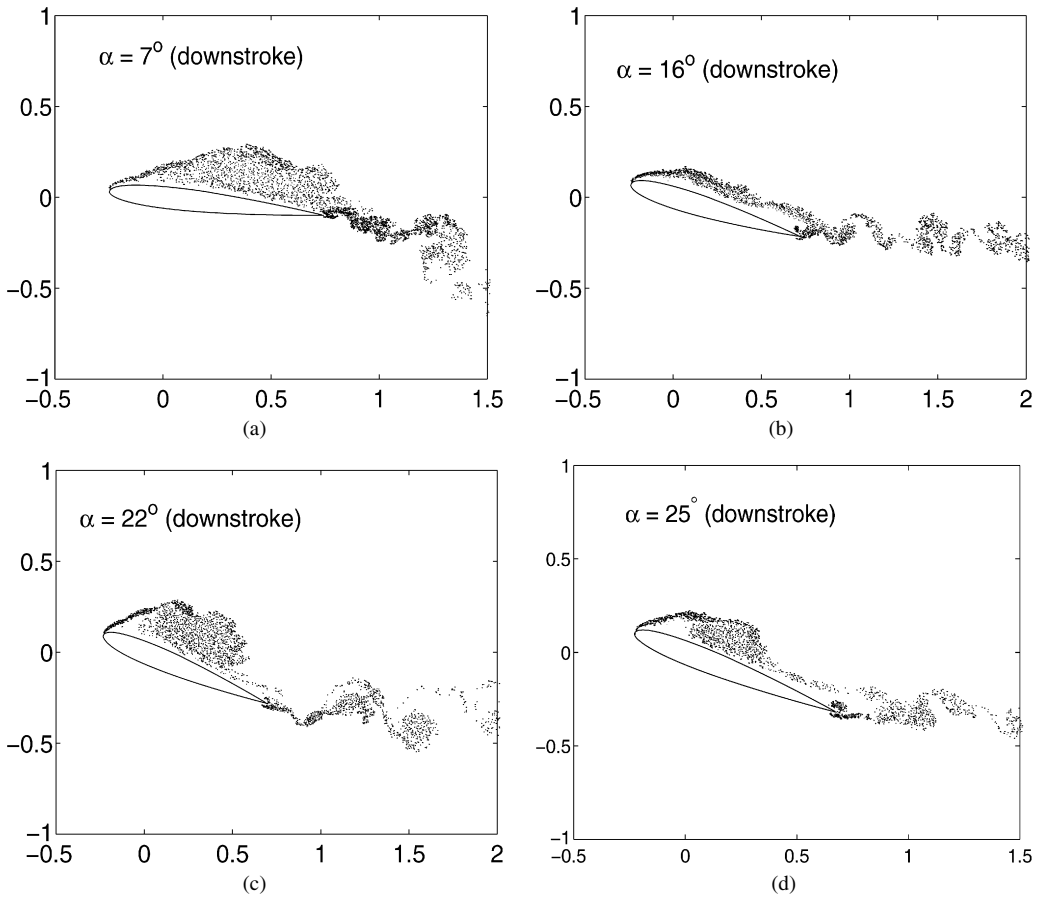

Fig. 4. Unsteady flow past airfoil pitching sinusoidally (downstroke). $\alpha(t) = 15 - 10\cos(\omega t)$ (cycle 2); $k = 0.5$; $Re = 10^4$; $a = -1/4$.

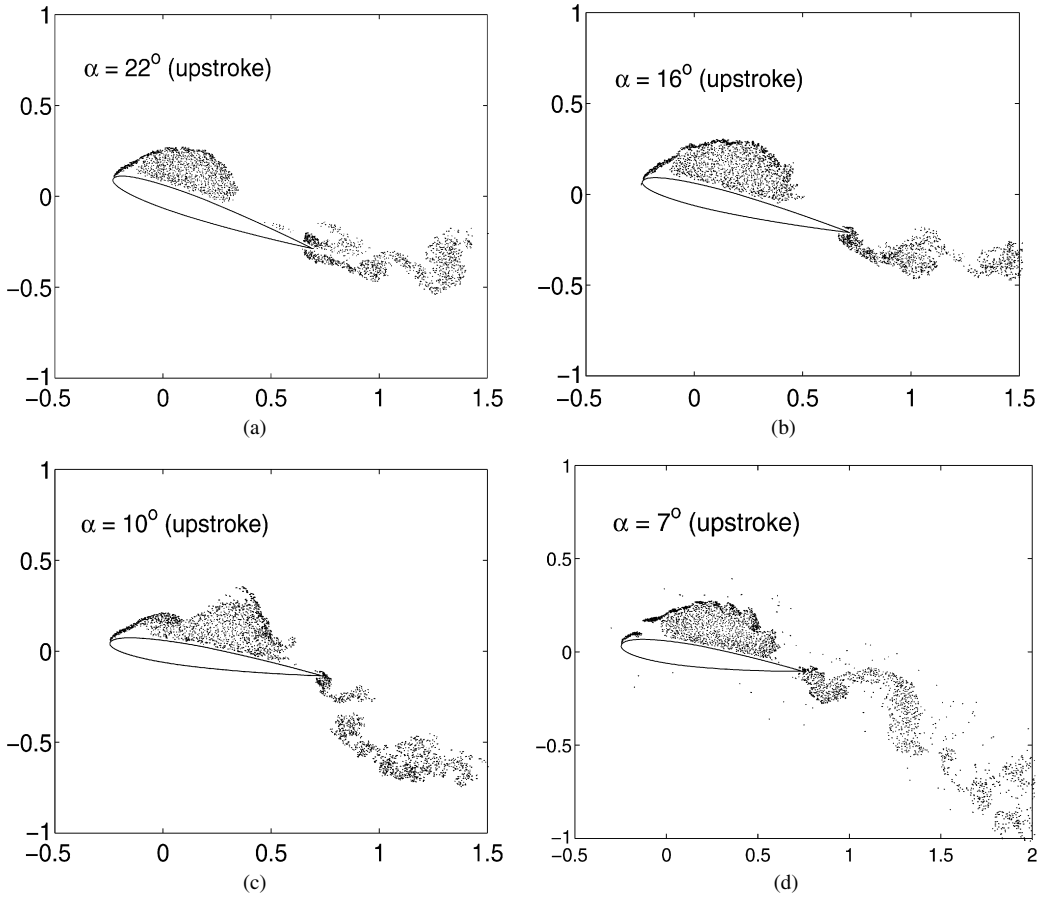

Fig. 5. Unsteady flow past airfoil pitching sinusoidally (upstroke). $\alpha(t) = 15 - 10\cos(\omega t)$ (cycle 2); $k = 0.5$; $Re = 10^4$; $a = -1/4$.

The relationship between the vorticity and the stream function is given by the Poisson equation

$$\nabla^2 \psi = -\Omega, \tag{3}$$

where ψ is the stream function. In this representation, the far-field boundary condition that the flow remains undisturbed needs to be carefully dealt with during numerical implementation [14].

The relationship between the vorticity and the velocity field is given by a vector Poisson equation [13,15]

$$\nabla^2 \vec{V} = -\nabla \times \vec{\Omega}. \tag{4}$$

The solution to this vector Poisson equation with appropriate boundary condition uniquely defines the velocity–vorticity relationship, and is expressed as an integral representation that is similar to the Bio–Savart law of electromagnetic theory [13,15,12]. Now the velocity field is determined from the known vorticity distribution in the fluid region R, as well as the velocity boundary conditions on the surface S of the solid body as well as the far-field. This integral relation is given by [15]

$$\vec{V}(\vec{r}, t) = -\frac{1}{2\pi}\left[\int_{\mathrm{R}} \frac{\vec{\Omega} \times (\vec{r}_0 - \vec{r})}{|\vec{r}_0 - \vec{r}|^2}\,\mathrm{dR} + 2\int_{\mathrm{S}} \frac{\vec{\Omega}_b \times (\vec{r}_0 - \vec{r})}{|\vec{r}_0 - \vec{r}|^2}\,\mathrm{dS} + \vec{V}_\infty\right], \tag{5}$$

where $\vec{\Omega}_b$ is the rigid body angular velocity of the solid whose boundary is denoted by S, and $\vec{V}_\infty$ its translational velocity. $\vec{r}_0$ is the vector distance from the origin of the reference frame to the vortex particles in the fluid region R, and $\vec{r}$ is the point in the flow-field where the induced velocity due to these vortex particles are to be determined. Note that the velocity field automatically satisfies the far-field velocity boundary condition of the flow.

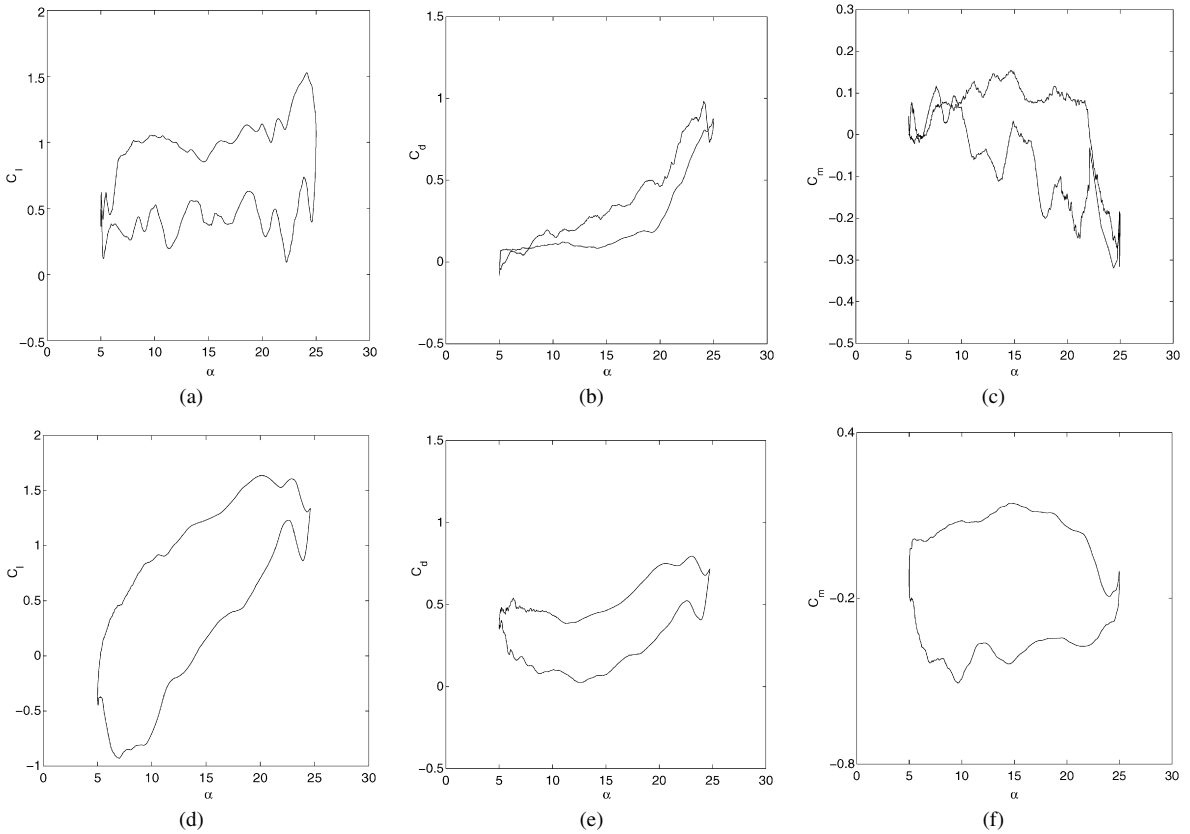

Fig. 6. Lift and drag coefficients as a function of angle-of-attack for sinusoidally pitching airfoil. $\alpha(t) = 15 - 10\cos(\omega t)$; $Re = 10^4$; $a = -1/4$; (a)–(c) $k = 0.5$, (d)–(f) $k = 1.0$.

New vortices are created at the body boundary by satisfying the 'no slip' and 'no penetration' boundary condition. The near-field boundary condition at the body surface states,

$$\vec{V} = \vec{V}_b(s), \tag{6}$$

where, $\vec{V}_b(s)$ represents the velocity of the body surface. In the present formulation, no-penetration condition is used to determine the body-bound vorticity distribution [10,15,16]. In order to satisfy no-slip, free vortices are generated at the body surface.

The discrete vortex numerical simulation that we have used in this study will use the vorticity evolution equation (2) together with the relation for the velocity field in terms of the vorticity given by Eq. (5).

Eq. (2) can be split into convection and diffusion parts and can be solved sequentially. This is known as operator splitting [11]. Thus, Eq. (2) can be represented as

$$\frac{\partial \Omega}{\partial t} + \vec{V} \cdot \nabla \Omega = 0, \tag{7}$$

$$\frac{\partial \Omega}{\partial t} = \nu \nabla^2 \Omega. \tag{8}$$

The convection equation (7) shows the invariance of vorticity of the vortex particles as they move with the fluid. The convection velocity is the same as that given by the Bio–Savart law. At each time step, only the velocity at the vortex location is needed to advance the simulation. An explicit first-order time marching scheme has been seen to be giving good result with a suitable choice of time step size.

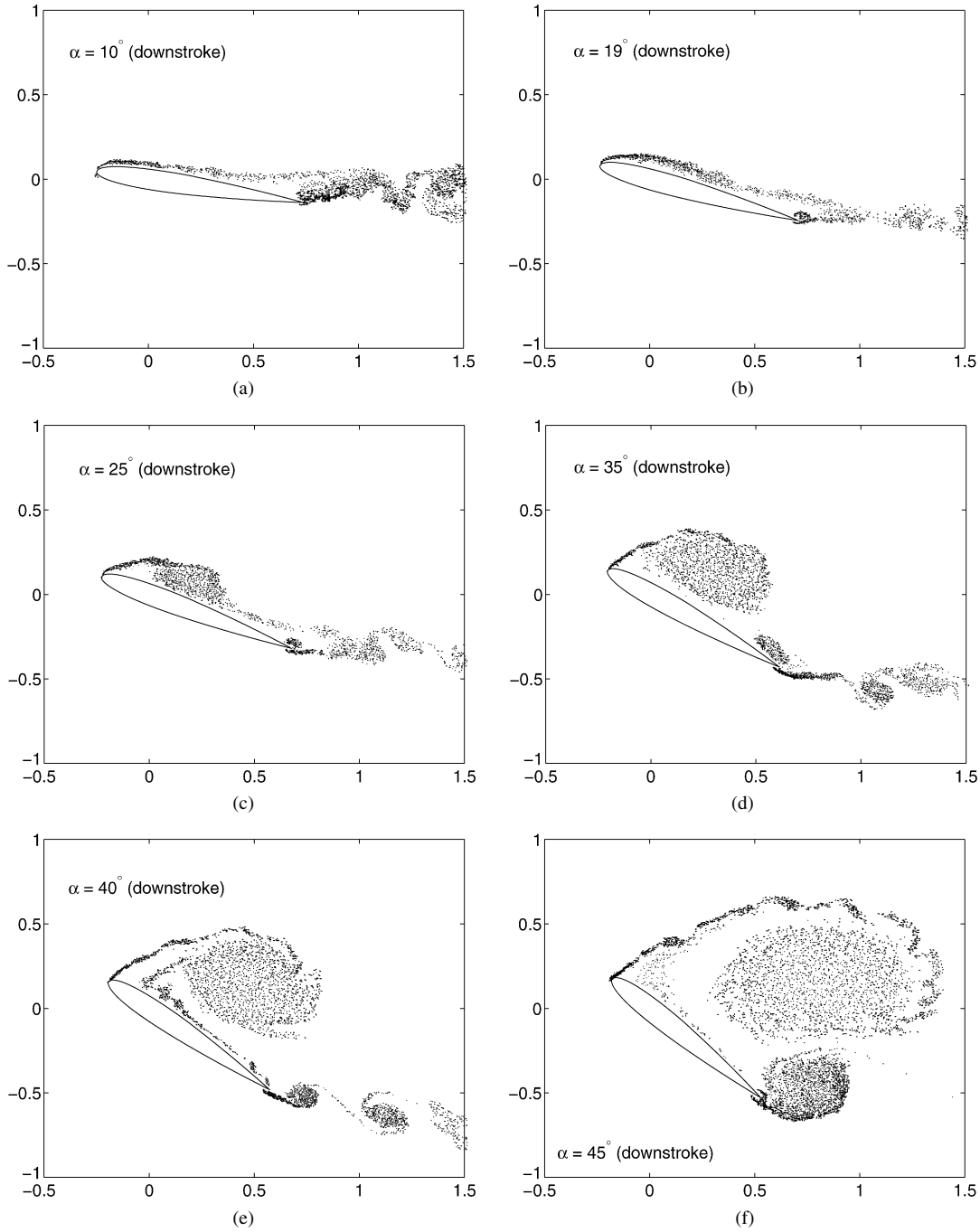

Fig. 7. Unsteady flow past airfoil pitching sinusoidally (downstroke). $\alpha(t) = 25 - 20\cos(\omega t)$ (cycle 2); $k = 0.5$; $Re = 10^4$; $a = -1/4$.

The solution of the diffusion part Eq. (8) is given by a Gaussian probability density function [13]. A random walk algorithm [11] is used to approximate diffusion. Further discussion on the random walk based vortex methods is given in [17,18].

The two-dimensional body surface is divided into a number of straight line panels, with the collocation point at the center of each panel. A vortex node is designated at each panel midpoint. A thin region near the body is regarded as a special control zone [12] where nascent vortices are created at each panel. After the convection and diffusion of these

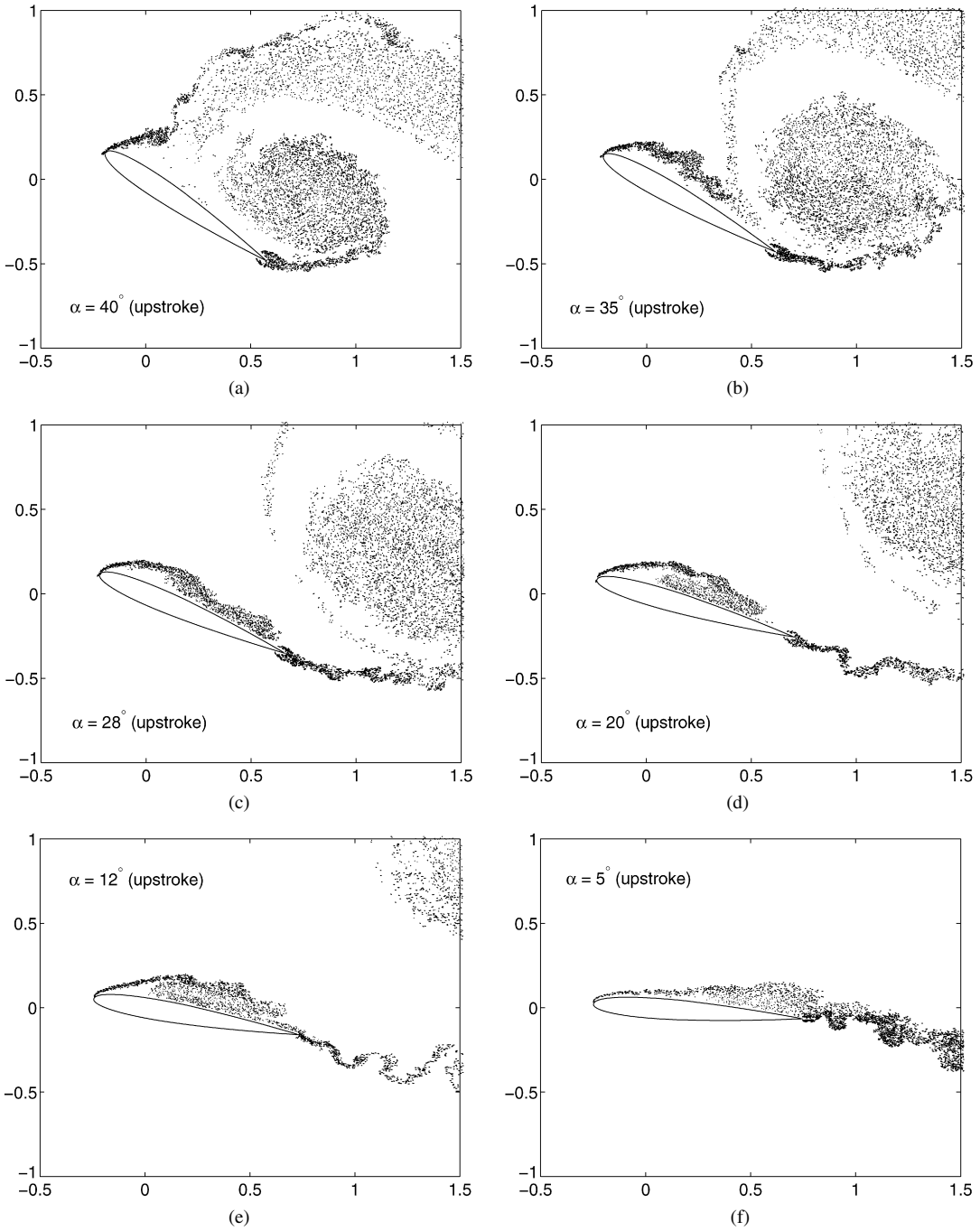

Fig. 8. Unsteady flow past airfoil pitching sinusoidally (upstroke). $\alpha(t) = 25 - 20\cos(\omega t)$ (cycle 2); $k = 0.5$; $Re = 10^4$; $a = -1/4$.

newly created vortices, those which remain inside this zone are again summed up and redistributed panel-wise, to be combined with the set of new panel vortices at the next time step.

The solution of this unknown vortex sheet is obtained by assuming the no-normal flow condition on the body surface, however, as there are no sources/sinks present in the flow, one equation in this set is redundant. The last equation required to make the set unique is obtained by satisfying Kelvin's theorem [12]. Thus, we have,

$$(\vec{V} - \vec{V}_b) \cdot \hat{n} = 0, \tag{9}$$

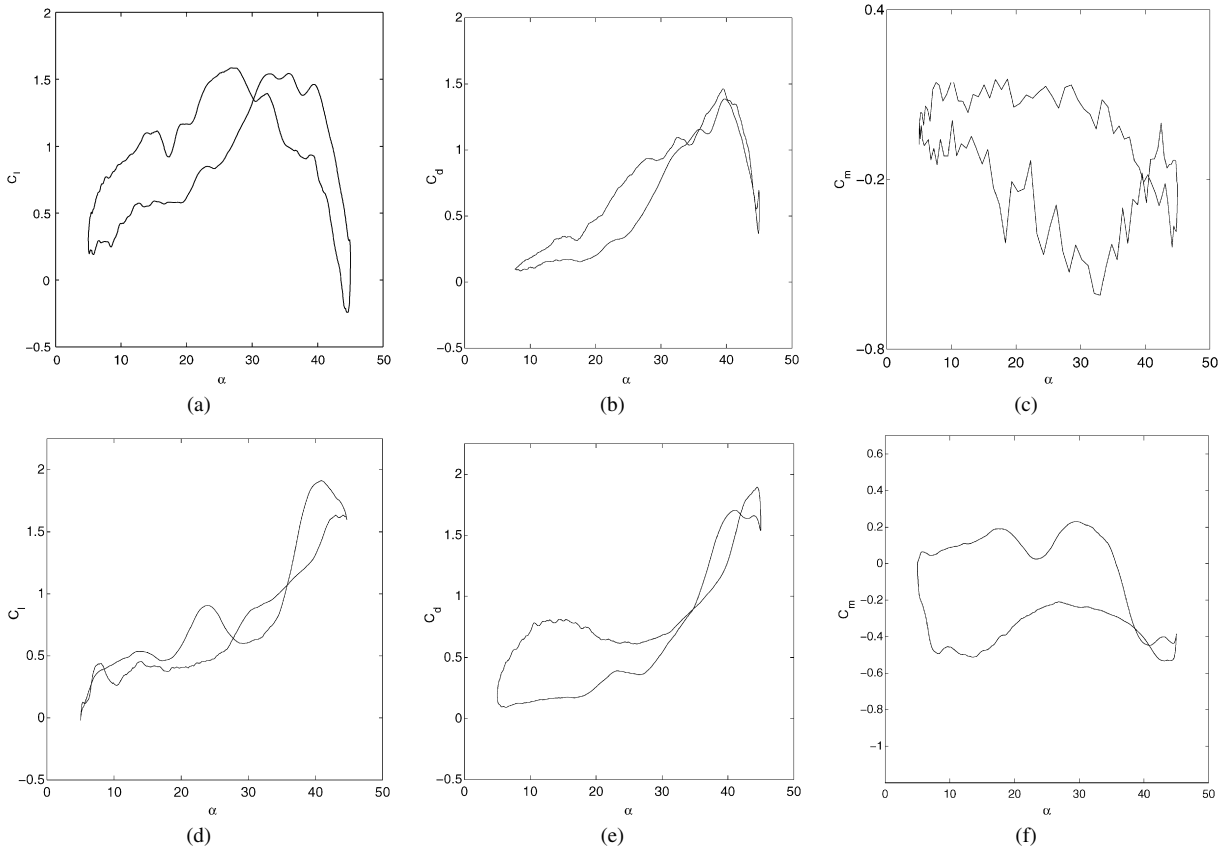

Fig. 9. Lift and drag coefficients as a function of angle-of-attack for sinusoidally pitching airfoil. $\alpha(t) = 25 - 20\cos(\omega t)$; $Re = 10^4$; $a = -1/4$; (a)–(c) $k = 0.5$, (d)–(f) $k = 1.0$.

where $\hat{n}$ denotes the normal vector to the body boundary. This body bound vortex sheet, in general, will not satisfy the no-slip condition. Therefore, the non-zero tangential velocity is nullified by generating free vortices at the surface. The vorticity flux of this free vorticity in the normal direction to the body surface is given by [19–21]

$$\nu \frac{\partial \Omega}{\partial \hat{n}}(s) = -\gamma(s)/\delta t, \tag{10}$$

where the left-hand side is the local vorticity flux, $\gamma(s)$ is the vortex sheet strength as a function of path length s along the boundary, and δt is the time interval. The vorticity flux is assumed to be constant over time interval δt.

Each surface panel is further subdivided into a number of sub panels and after the creation of the vortices at each panel, they are broken down into vortex blobs at each of the sub panels [12]. These blobs are later convected and diffused. Each blob is assumed to have symmetrical vorticity distribution and defined by a core function [11].

The forces exerted on the body comes from the surface pressure and the surface friction. The tangential pressure gradient on the body surface is given by,

$$\frac{1}{\rho}\frac{\partial p}{\partial \hat{s}} = -\hat{s} \cdot \frac{D\vec{V}_b}{Dt} - \hat{n} \cdot \vec{r}\frac{D\Omega_b}{Dt} + \hat{s} \cdot \vec{r}\Omega_b{}^2 + \nu \frac{\partial \Omega}{\partial \hat{n}}, \tag{11}$$

where, Ω_b is the angular velocity of the body motion. Eq. (11) is integrated to calculate the aerodynamic loads from the surface pressure distribution.

3. Discussion

Numerical simulation of the unsteady, incompressible, viscous flow past a sinusoidally oscillating airfoil in the post-stall regime has been performed using the method of discrete vortices. The airfoil oscillates about its quarter-

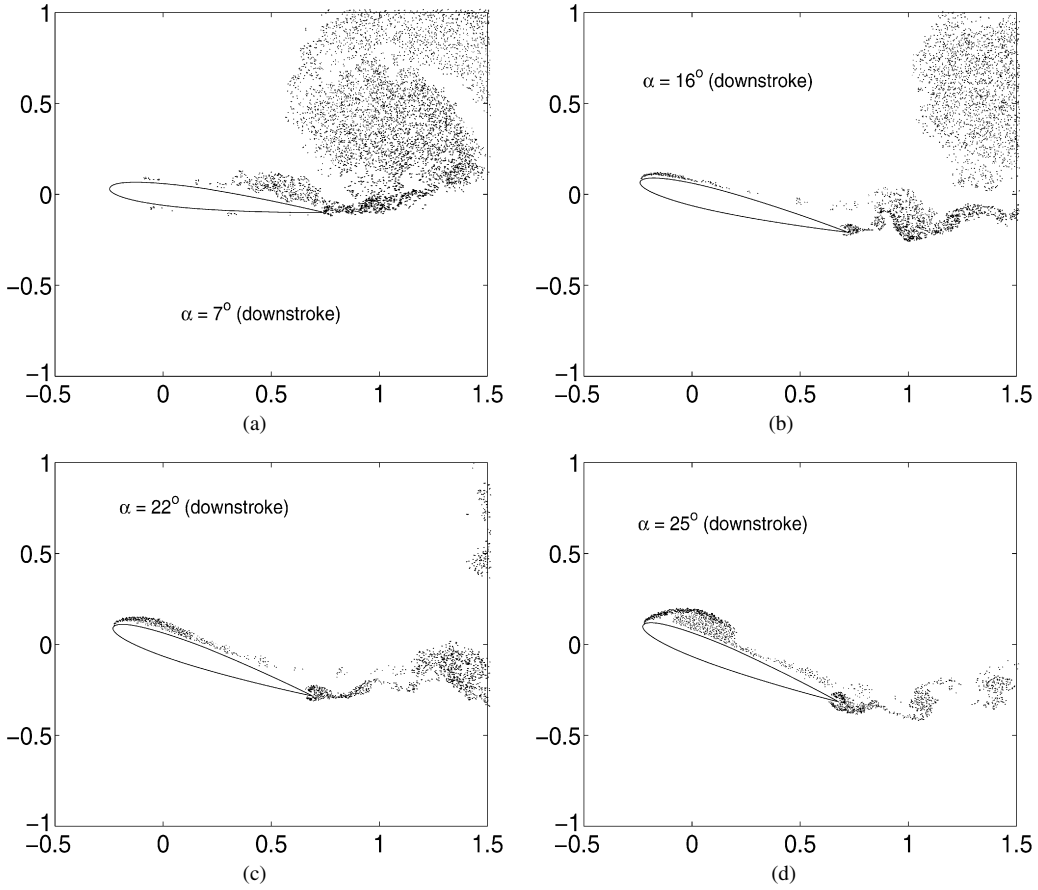

Fig. 10. Unsteady flow past airfoil pitching sinusoidally (downstroke). $\alpha(t) = 15 - 10\cos(\omega t)$ (cycle 3); $k = 1.5$; $Re = 10^4$; $a = -1/4$.

chord point. The study uses 80 panels with 5 sub panels in each of them. This makes a total of 400 vortices generated at any time-step. The airfoil chord length $c = 1$, cut-off $\sigma = 0.0045$, and control zone thickness $\Delta = 0.0135$. These values were finalized after some trial and error, and validation of results with the available literature. An important entity which can control the accuracy of the numerical scheme is the time interval. As we have already seen in Eq. (10), the time step size should be small enough to ensure that the vorticity flux generated from the body can be assumed to be constant over the interval. The time marching process relies on an explicit first order Eulerian scheme. The time step size used in the simulation is $\Delta t = 0.01$ seconds. This choice fulfills the criteria of the stability of the time integration and the frequency of oscillations; this time step also gives convergence to the scheme itself along with two other parameters, the control zone thickness and the number of vortices created during the time interval. One should be careful about choosing the number of vortices generated at each time step. A hugely overestimated vortex point representation can be severely wrong, and too few a number of vortex particles in the flow field may be insufficient to accurately simulate the true physical phenomenon. For example, too small a time step size may restrain the nascent vortices from entering the flow field after crossing the control zone. In that case, if more number of vortices are generated per step, it may counter this effect to some extent. Also, manipulating the thickness of the control zone can be useful. Thus, the time step size, the control zone thickness and the number of vortices generated, are somewhat mutually dependent.

The random discrete vortex method is a well established technique. The validation of the simulation code was done by comparing the results with experimental observations. Our results have compared well with the experiments reported by Walker et al. [22] and Francis and Keesee [23], for an airfoil rapidly pitching at constant rates. As an example, we present some snapshots from our discrete vortex simulations with a nondimensional pitch rate of $\dot{\alpha}c/V_\infty = 0.2$ and $Re = 4.5 \times 10^4$, and compare with the experimental results of [22]. The experimental vorticity patterns [22] have

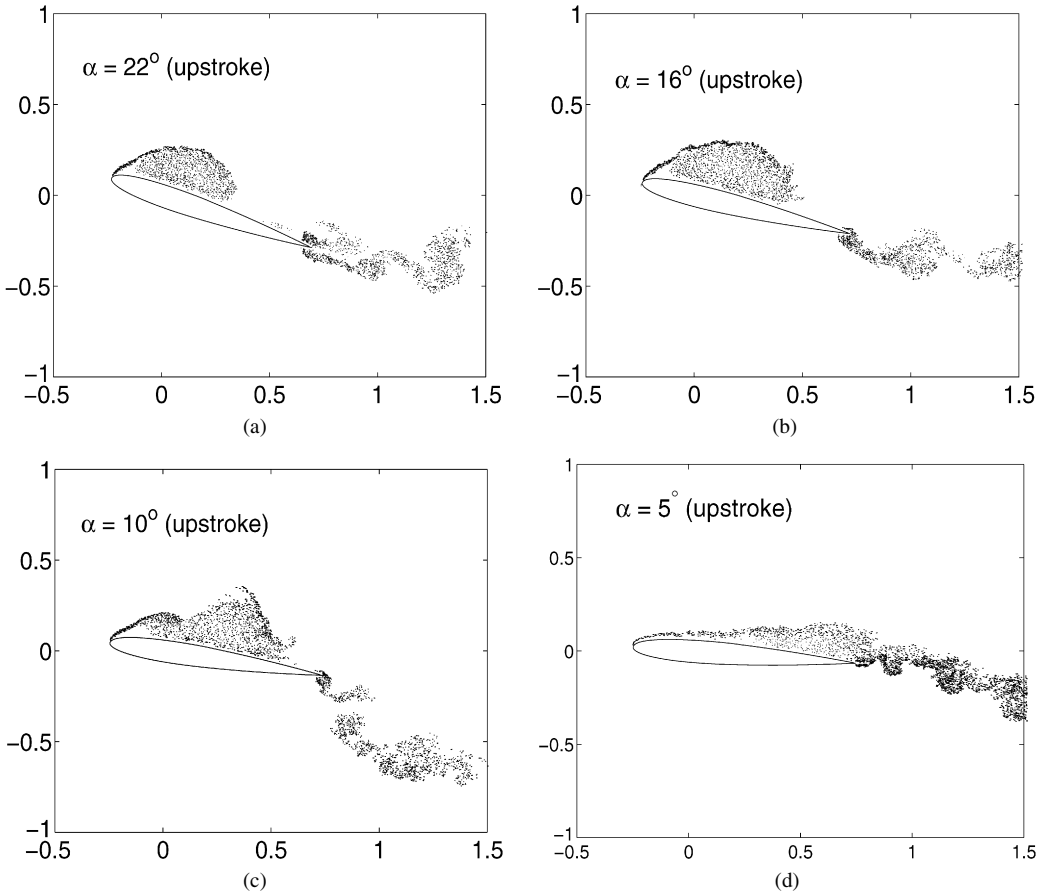

Fig. 11. Unsteady flow past airfoil pitching sinusoidally (upstroke). $\alpha(t) = 15 - 10\cos(\omega t)$ (cycle 3); $k = 1.5$; $Re = 10^4$; $a = -1/4$.

been shown in Fig. 1 and the discrete vortex simulations have been presented in Fig. 2. As evident from these plots, the match is quite well. Walker et al. [22] have not given the load coefficient values. The experimental load coefficients for the same case was reproduced in [2], from where we take the C_l plot and draw the numerical lift coefficient obtained by the discrete vortex simulation in Fig. 3. Once again, the simulation results follow the experimental trend quite well. We have also compared discrete vortex simulations for sinusoidally oscillating airfoil cases, for example, with the results presented by Akbari and Price [9].

In this work we consider a NACA 0012 airfoil oscillating in pitch (α) degree-of-freedom in the following time dependent fashion:

$$\alpha(t) = \alpha_m - \alpha_0 \cos(\omega t). \tag{12}$$

We start the simulations with the following parameters.

$\alpha_m = 15°$, $\alpha_0 = 10°$, reduced frequency $k = \omega c/V_\infty = 0.5$–$3.0$ and $Re = 1 \times 10^4$. Akbari and Price [9] have presented dynamic stall results at the same mean and amplitude of angle of attack but only up to $k = 1.0$. Vortex patterns obtained by discrete vortex method at different time instances during the dynamic stall cycle compare well with their results for $k = 0.5$ and 1.0. However as k is increased beyond that, a period doubling behavior in the vortex pattern is seen. This is also reflected on the load coefficient time history. We discuss various reduced frequency cases below. In the next part of the study, both the mean and amplitude of the pitch motion are increased to 25° and 20°, respectively. This in turn increases the maximum angle of attack during one dynamic stall cycle from 25° to 45°. The reduced frequencies are varied as in the previous case, between 0.5 and 3.0. We discuss the similarities and differences in the vortex growth and shedding patterns at the same reduced frequency values but different pitch angle cases. With a time step size of 0.01, the number of time steps per cycle for the smallest reduced frequency (0.5) is 1257 and for the largest reduced frequency (3.0) is 210 approximately, which is large enough even for the fastest motion.

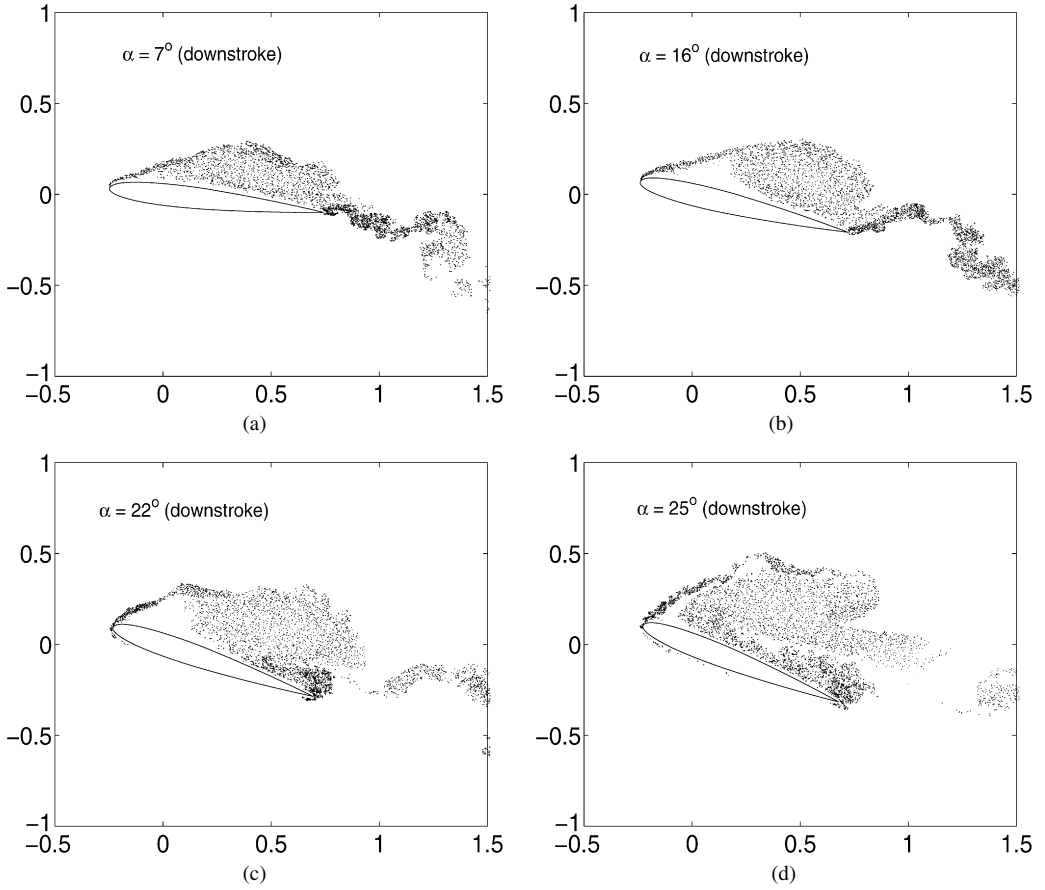

Fig. 12. Unsteady flow past airfoil pitching sinusoidally (downstroke). $\alpha(t) = 15 - 10\cos(\omega t)$ (cycle 4); $k = 1.5$; $Re = 10^4$; $a = -1/4$.

3.1. $k = 0.5, 1.0$

We present the vortex pattern snapshots at various instances of a dynamic stall cycle for $k = 0.5$ case. Fig. 4 presents the downstroke half cycle for $\alpha = 15° - 10°\cos(\omega t)$ and Fig. 5 presents the upstroke half cycle. The cycle starts at 5°, nose up position. By 'downstroke' half cycle we mean, during the time the trailing edge of the airfoil goes down with respect to the axis of rotation, thus increasing the angle of attack from the minimum to the maximum value. At $\alpha = 7°$, the flow is not fully attached to the body and there are significant vortices present in the near wake. These are due to the separation and vortex shedding during the previous cycle. As the downstroke continues, the flow becomes more attached as seen in Fig. 4(b). Later, clockwise leading edge vortex develops and grows. At $\alpha = 22°$ (downstroke), the leading edge vortex covers most part of the body surface. At this angle of attack, there is also a reverse flow region from the trailing edge towards the leading edge. At $\alpha = 25°$ (downstroke), the leading edge vortex separates itself from the body. There is also a trace of a developing trailing edge anti-clockwise vortex at this angle. The upstroke half of the cycle is shown in Fig. 5. At $\alpha = 22°$ (upstroke), the trailing edge vortex have grown considerably and the shed leading edge vortex is seen to be convected downstream. During the upstroke, another vortical structure is developed on the surface and is shed in the wake. Part of this vortical structure remains close to the body till the end of the upstroke and is thus responsible for the flow not being attached to the body at the end of the cycle. However, the flow gradually re-attaches itself during the first half of the next cycle's downstroke as the small vortices are carried downstream. Fig. 6(a), (b) and (c) shows the aerodynamic lift, drag and moment coefficients during the second cycle. The lift force takes the maximum value at around pitch angle 25° and then sharply falls. The drag force also gradually falls at the start of the upstroke. This decrease in the load coefficients coincides with the shedding of the fully developed leading edge vortex.

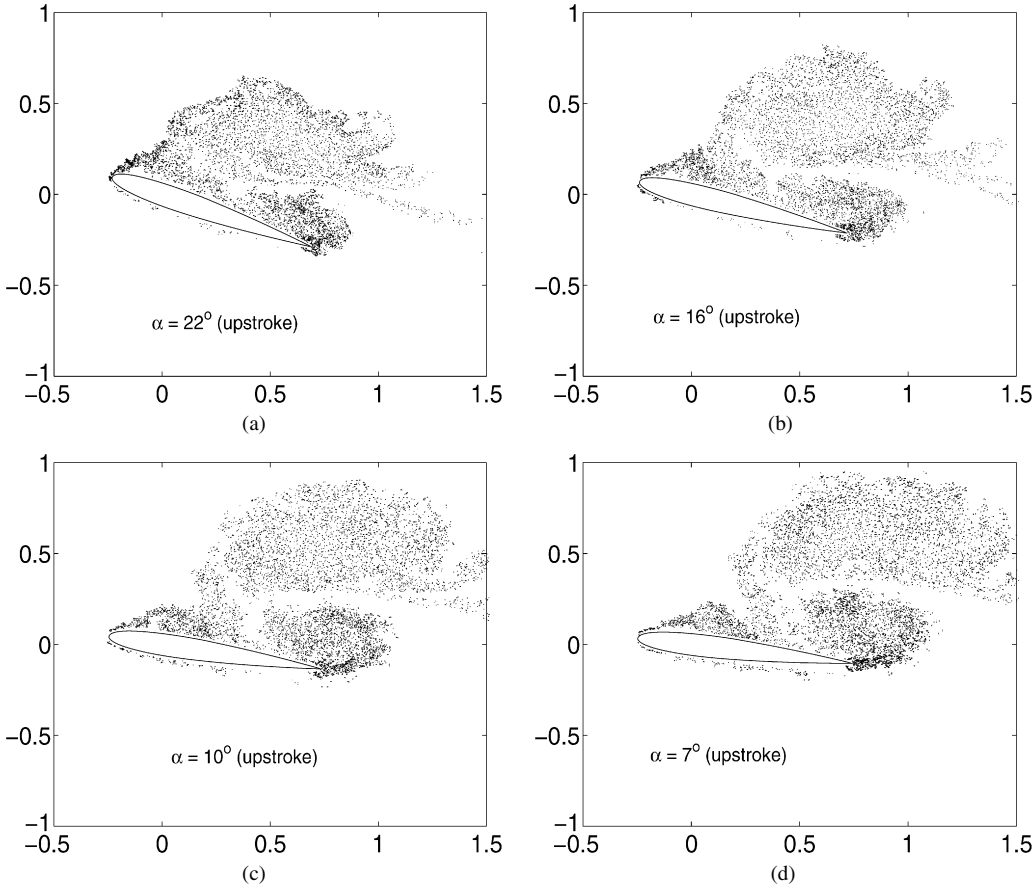

Fig. 13. Unsteady flow past airfoil pitching sinusoidally (upstroke). $\alpha(t) = 15 - 10\cos(\omega t)$ (cycle 4); $k = 1.5$; $Re = 10^4$; $a = -1/4$.

Next, we vary the angle of attack in the range of 5° to 45°, in order to increase the maximum value of incidence the airfoil can attain. The behavior and growth of dynamic stall vortex is dependent on many parameters, the maximum angle of attack attained by the airfoil during its periodic movement is evidently one of them. It is also apparent that the size and movement of the leading edge vortex is mostly responsible for the aerodynamic load history during dynamic stall. Fig. 7 shows the snapshots during the downstroke of the second cycle of the airfoil pitch motion $\alpha = 25° - 20°\cos(\omega t)$; $k = 0.5$. At the beginning of the downstroke, the flow is not fully attached at the trailing edge owing to the vortices created and shed during the previous cycle. As the downstroke angle increases, a leading edge vortex grows at the upper surface. At around $\alpha = 35°$, it is quite well developed and near the surface. Around $\alpha = 40°$, a reverse flow develops from the trailing edge towards the leading edge and the leading edge vortex has already started moving away from the upper surface. At the end of the downstroke, the leading edge vortex has moved further and a counter-clockwise trailing edge vortex starts to develop. During the upstroke, shown in Fig. 8, as the leading edge vortex moves off the airfoil surface and is shed into the wake, the trailing edge vortex grows and is shed around $\alpha = 28°$. Around this angle of attack, a second and small vortex like structure is seen on the upper surface which subsequently moves towards the trailing edge. At the end of the upstroke, a re-attachment process starts from the leading edge downwards. At the end of the upstroke the flow is almost attached, except at the trailing edge. The load coefficients are shown in Fig. 9(a), (b) and (c). Maximum lift during the downstroke half-cycle occurs between $\alpha = 35°$–$40°$ when the leading edge vortex is quite well developed and close to the body and then it falls sharply before rising again during the upstroke. The falling off of the lift curve during the upstroke coincides with the shedding of the trailing edge vortex. The drag time history also follows almost the same pattern.

For $k = 1.0$, with both pitch angle cases, dynamic vortex behavior is again single periodic like the previous case. For the higher pitch angle case, the vortices are more well developed and stronger which affects the load coefficients

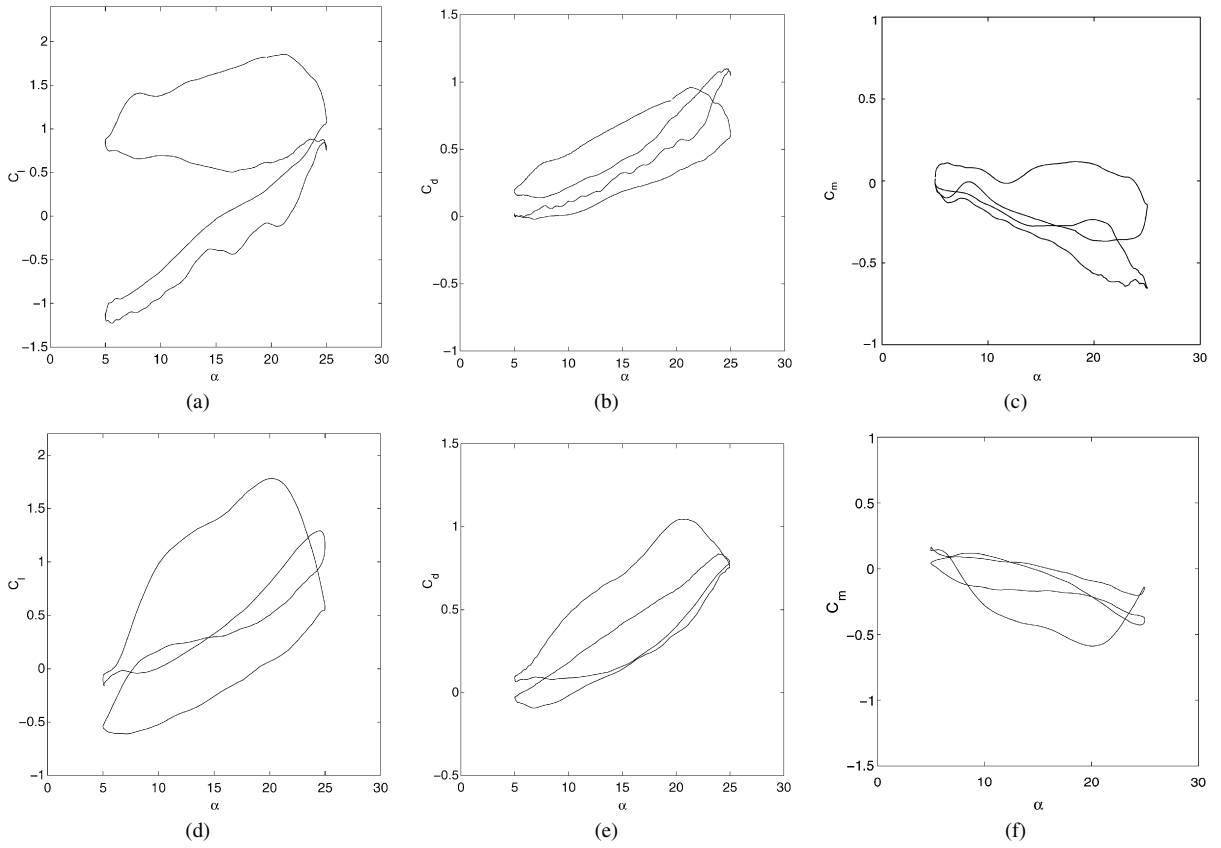

Fig. 14. Lift and drag coefficients as a function of angle-of-attack for sinusoidally pitching airfoil. $\alpha(t) = 15 - 10\cos(\omega t)$; $Re = 10^4$; $a = -1/4$; (a)–(c) $k = 1.5$, (d)–(f) $k = 2.5$.

significantly. Therefore, the maximum aerodynamic loads for the later case is also higher, as shown in Fig. 9(d)–(f). This is compared to the load coefficients shown in Fig. 6(d)–(f).

3.2. $k = 1.5, 2.0, 2.5$

For the lower pitch angle case of $\alpha = 15^\circ - 10^\circ\cos(\omega t)$, increasing the frequency further to $k = 1.5$, a period doubling effect was observed. We present the vortex patterns at two consecutive cycles of the harmonic motion. The vortex patterns during the third and fourth pitch cycles are similar to that at the first and second cycles. Their vortex patterns are shown in Figs. 10–13. During the downstroke of the third oscillation cycle, as shown in Fig. 10, a flow reattachment process takes place and a leading edge vortex gradually develops towards the end of the downstroke. At the start of the downstroke, the near wake region flow is still vortical due to the trailing edge vortex which was shed during the upstroke of the previous wake. Later these vortices are carried away from the body as the leading edge vortex slowly builds up. During the upstroke of the third cycle, as shown in Fig. 11, the leading edge vortex further grows and has traveled almost till the trailing edge along the upper surface by the end of the upstroke. The next, or the fourth, cycle is very interesting and quite different from that of the earlier frequency cases, from the point of view of the leading edge vortex behavior. After covering the upper surface of the body the leading edge vortex starts separating from the leading edge region. This is clearly evident in Fig. 12(b) and (c). Moreover, at $\alpha = 22^\circ$, a reverse flow from the trailing edge towards the leading edge can be observed. This reverse flow region separates the rear part of the leading edge from the body, seen in Fig. 12(d). The upstroke of the fourth cycle is shown in Fig. 13. During the upstroke the leading edge vortex is finally separated and advected away from the body. A trailing edge vortex grows till $\alpha = 7^\circ$, shown in Fig. 13(d). This trailing edge vortex is then shed in the wake after the leading edge vortex. Another small leading edge vortical formation has also been formed by this time which travels along

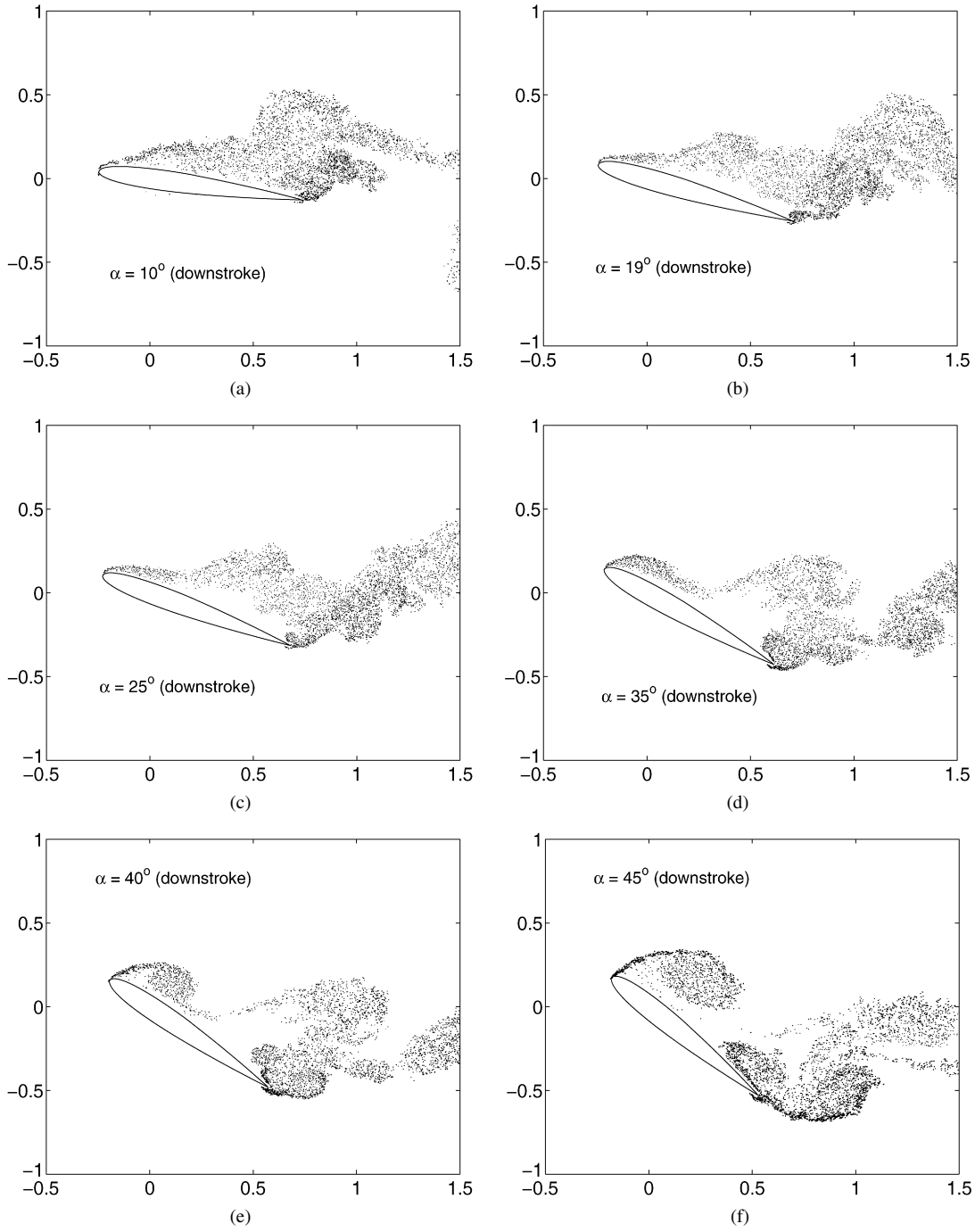

Fig. 15. Unsteady flow past airfoil pitching sinusoidally (downstroke). $\alpha(t) = 25 - 20\cos(\omega t)$ (cycle 3); $k = 1.5$; $Re = 10^4$; $a = -1/4$.

the upper surface towards the trailing edge. This vortical formation traveling towards the trailing edge was seen in Fig. 10(a) before it was also shed in the wake. The load coefficients have been shown in Fig. 14(a)–(c). The third and fourth cycles of the loading history describe a double loop in the response time history, that clearly indicates a period doubling response behavior. At $k = 2.0$ and 2.5, the vortex growth and shedding patterns are not only double periodic like $k = 1.5$ case, but also the sequence of events of the vortex behavior are also similar. Growth of the leading edge vortex during almost the entire third cycle and then its shedding during the fourth cycle have been

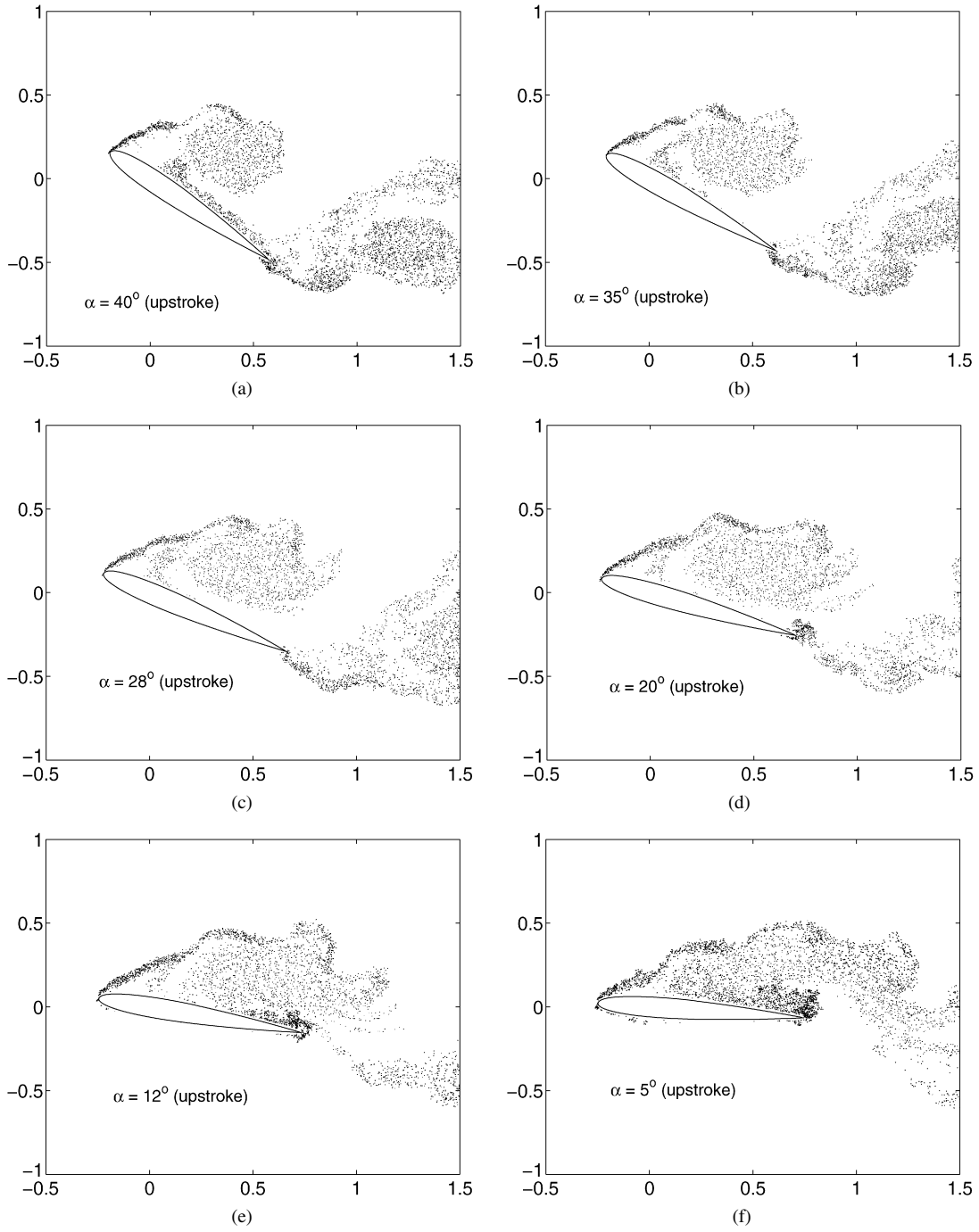

Fig. 16. Unsteady flow past airfoil pitching sinusoidally (upstroke). $\alpha(t) = 25 - 20\cos(\omega t)$ (cycle 3); $k = 1.5$; $Re = 10^4$; $a = -1/4$.

observed for the other two k cases as well. However, the shape of the load coefficient curves are not exactly alike. Load coefficient plot for $k = 2.5$ case has been presented in Fig. 14(d)–(f). Though the shapes are different, one can see that the maximum values are nearby. The maximum lift occurs around an angle of attack of 20°, for both the cases.

Next, we discuss the higher angle of attack case of $\alpha = 25° - 20°\cos(\omega t)$ for $k = 1.5$. Vortex patterns at the third cycle has been presented. Few downstroke snapshots have been shown in Fig. 15. At the beginning of the down-

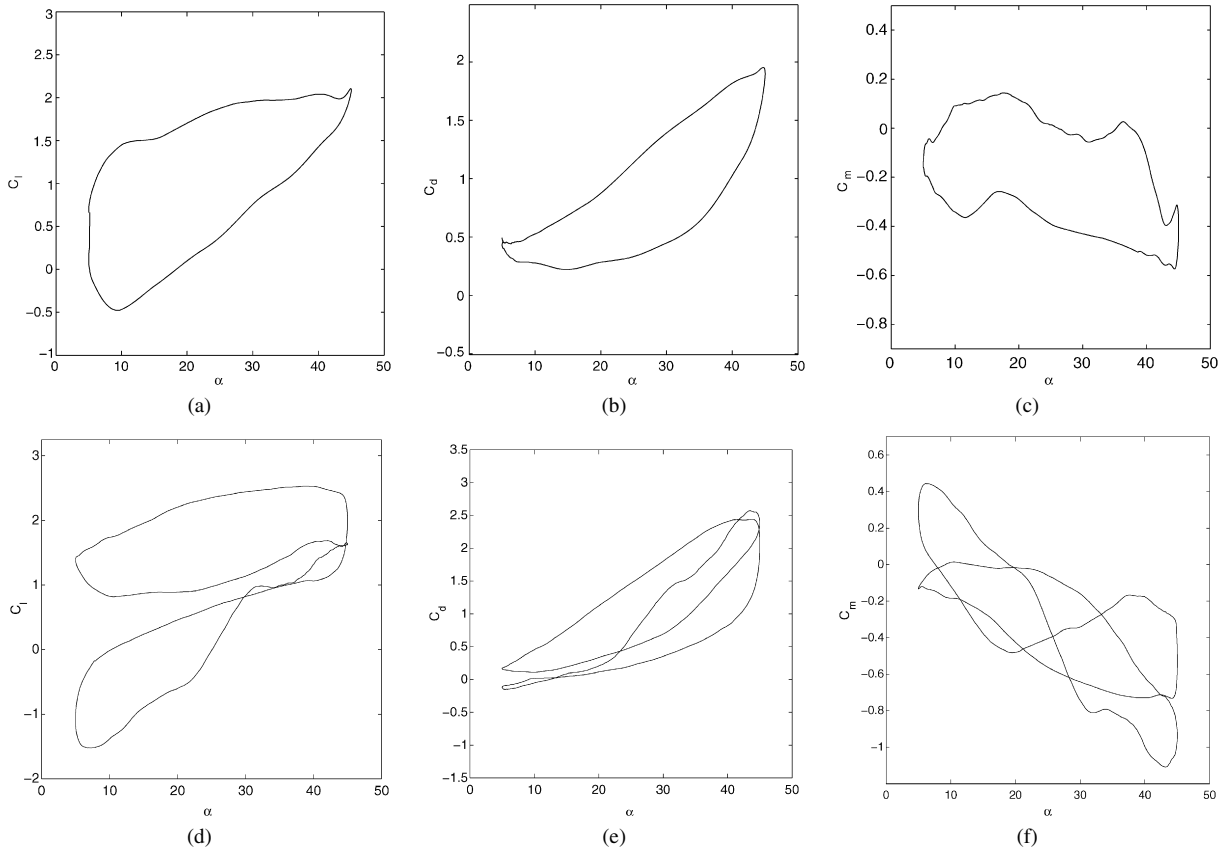

Fig. 17. Lift and drag coefficients as a function of angle-of-attack for sinusoidally pitching airfoil. $\alpha(t) = 25 - 20\cos(\omega t)$; $Re = 10^4$; $a = -1/4$; (a)–(c) $k = 1.5$, (d)–(f) $k = 2.0$.

stroke, the flow near the body is substantially vortical due to vortices shed during the previous cycle's upstroke. As the downstroke progresses, a reattachment region starts from the leading edge. The vortical region near the body also moves away from the body. Also, a trailing edge vortex develops gradually. Around $\alpha = 40°$, a leading edge vortex also starts to develop. This is seen growing till the end of the downstroke. The upstroke half cycle is depicted in Fig. 16. At the beginning the leading edge vortex grows for a while and also a reverse flow region is seen from the trailing edge towards the leading edge. This helps the leading edge vortex to gradually move away from the body. The trailing edge vortex is also shed in the wake around $\alpha = 40°$ (upstroke). For the rest of the upstroke, the leading edge vortical structure spreads and almost covers the full upper surface of the body even as staying slightly away from the surface. At around $\alpha = 12°$, a trailing edge vortex starts to develop and grows till the end of the upstroke. At the next downstroke this vortical structure will be shed. The leading edge vortex structure which is already shed will remain in the nearby wake, which was visible in the downstroke half cycle snapshots of Fig. 15. One can notice that the dynamics of the vortex structure is characteristically different here. The difference with the smaller pitch angle case is, the single periodic nature of the dynamic stall vortex. The vortex growth and shedding pattern repeats itself after one dynamic stall cycle. The load coefficients shown in Fig. 17(a)–(c) also shows a single loop. The maximum values of the lift and drag coefficients are higher than their low pitch angle counter parts.This could be attributed to the stronger vortex structures that are developed for the higher angle case.

Next, as k increases further to $k = 2.0$ for the higher maximum angle of attack, a period doubling occurs. We present the load coefficient plots for that case in Fig. 17(d)–(f). As k value is increased further, a period doubling pattern is continuing at $k = 3.0$ case shown in Fig. 18(d)–(f). However, for the smaller pitch angle case, the vorticity dynamics comes back to a single periodic one, shown in Fig. 18(a)–(c).

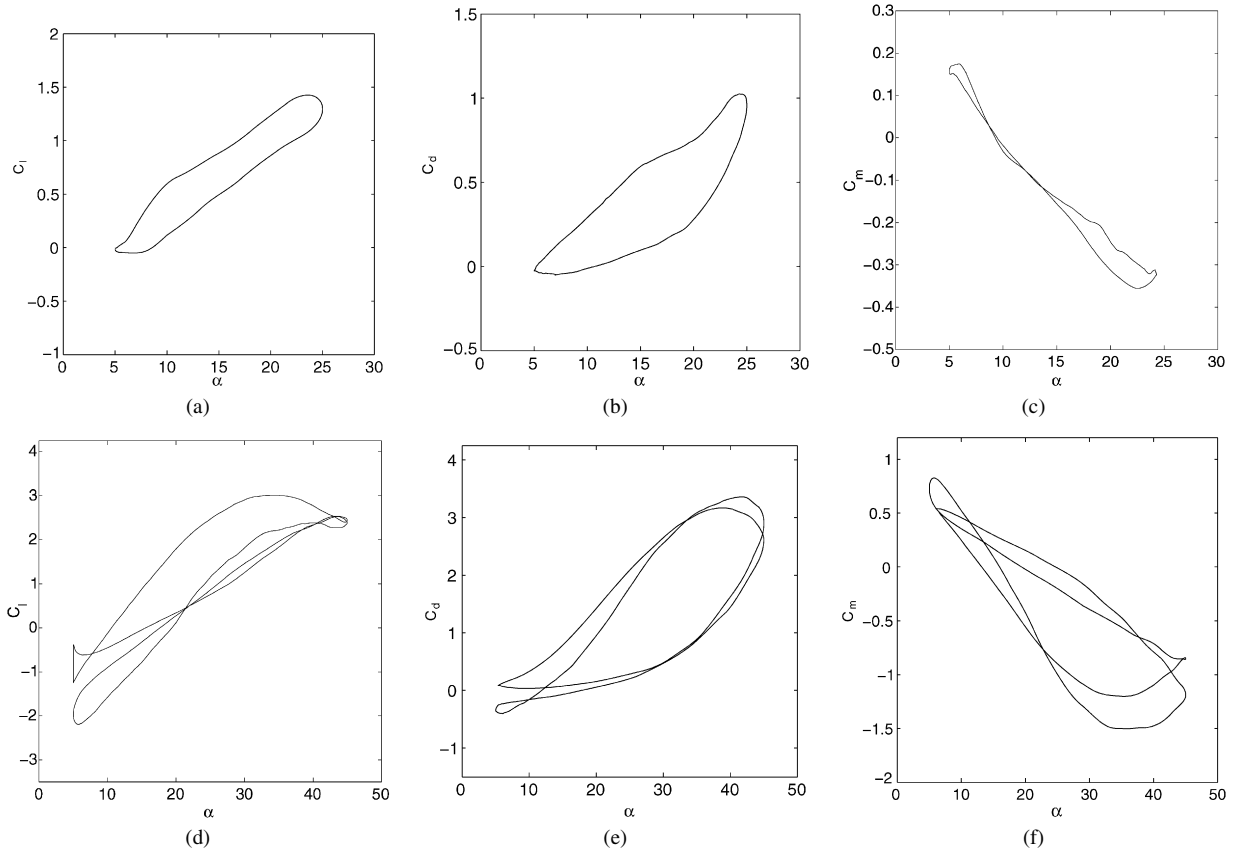

Fig. 18. Lift and drag coefficients as a function of angle-of-attack for sinusoidally pitching airfoil; $k = 3.0$; $Re = 10^4$; $a = -1/4$; (a)–(c) $\alpha(t) = 15 - 10\cos(\omega t)$, (d)–(f) $\alpha(t) = 25 - 20\cos(\omega t)$.

4. Summary and conclusions

Varying the pitching angle of an oscillating airfoil in the post stall regime impacts its dynamic stall behavior significantly. Most previous studies investigate the effects of varying the mean angle of attack and the amplitude of angle of attack independently. However, we consider the total angle of attack to be more important in influencing the growth of the leading edge vortex structure, which in turn affects the aerodynamic loading during dynamic stall. Therefore, we have changed both the mean and the amplitude to increase the total angular variation in pitch. We have simulated two different sinusoidal oscillation of a NACA 0012 airfoil. One makes the airfoil oscillate between 5° and 25°, the other between 5° and 45°. The oscillation frequency range has been same for both the cases. The higher maximum angle of attack allows the leading edge vortex to grow stronger. As a result, the lift, drag and moment coefficients show higher maximum values during the dynamic stall process. The general sequence of the vortex behavior at the same reduced frequencies also changes. Reduced frequency, which has been identified as a bifurcation parameter for the simulated nonlinear system, shows different period doubling bifurcation patterns for the two different pitch angle cases.

References

[1] L. Carr, Progress in analysis and prediction of dynamic stall, Journal of Aircraft 25 (1) (1988) 6–17.
[2] M. Visbal, J. Shang, Investigation of the flow structure around a rapidly pitching airfoil, AIAA Journal 27 (8) (1989) 1044–1051.
[3] M. Visbal, Dynamic stall of a constant rate pitching airfoil, Journal of Aircraft 27 (1990) 400–407.
[4] I. Tuncer, J. Wu, C. Wang, Theoretical and numerical studies of oscillating airfoils, AIAA Journal 28 (9) (1990) 1615–1624.
[5] K. Ohmi, M. Coutanceau, T. Loc, A. Dulieu, Vortex formation around an oscillating and translating airfoil at large incidence, Journal of Fluid Mechanics 211 (1990) 37–60.

[6] K. Ohmi, M. Coutanceau, O. Daube, T. Loc, Further experiments on vortex formation around an oscillating and translating airfoil at large incidence, Journal of Fluid Mechanics 225 (1991) 607–630.
[7] L.W. Carr, M.S. Chandrasekhara, Compressibility effects on dynamic stall, Progress in Aerospace Sciences 32 (1996) 523–573.
[8] J.A. Ekaterinaris, M.F. Platzer, Computational prediction of airfoil dynamic stall, Progress in Aerospace Sciences 33 (1998) 749–846.
[9] M. Akbari, S. Price, Simulation of dynamic stall for a naca 0012 airfoil using a vortex method, Journal of Fluids and Structures 17 (2003) 855–874.
[10] L. Qian, M. Vezza, A vorticity based method for incompressible unsteady viscous flows, Journal of Computational Physics 172 (2001) 515–542.
[11] A. Chorin, Numerical study of slightly viscous flow, Journal of Fluid Mechanics 57 (4) (1973) 785–796.
[12] H. Lin, M. Vezza, R. McD. Galbraith, Discrete vortex method for simulating unsteady flow around pitching aerofoils, AIAA Journal 35 (3) (1997) 494–499.
[13] G. Batchelor, An Introduction to Fluid Dynamics, Cambridge University Press, New Delhi, 1967.
[14] T. Tang, D.B. Ingham, On steady flow past a rotating circular cylinder at Reynolds numbers 60 and 100, Computers and Fluids 19 (1991) 217–230.
[15] J. Wu, J. Thompson, Numerical solutions of time-dependent incompressible Navier–Stokes equations using an integro-differential formulation, Computers and Fluids 1 (1973) 197–215.
[16] A. Leonard, in: T.B. Gatski, M.Y. Hussaini (Eds.), Simulation and Modeling of Turbulent Flows, Oxford University Press, London, 1996.
[17] A. Fogelson, R. Dillon, Optimal smoothing in function-transport particle methods for diffusion problems, Journal of Computational Physics 109 (1993) 155–163.
[18] D. Fishelov, A new vortex scheme for viscous flows, Journal of Computational Physics 86 (1990) 211–224.
[19] P. Koumoutsakos, A. Leonard, F. Pepin, Boundary conditions for viscous vortex methods, Journal of Computational Physics 113 (1994) 52–61.
[20] R.A. Schmall, R.B. Kinney, Numerical study of unsteady viscous flow past a lifting plate, AIAA Journal 12 (1974) 1566–1573.
[21] M.J. Lighthill, Laminar Boundary Layers, in: J. Rosenhead (Ed.), Oxford University Press, New York, 1963.
[22] J. Walker, H. Helin, J. Stricklan, An experimental investigation of an airfoil undergoing large-amplitude pitching motions, AIAA Journal 23 (8) (1985) 1141–1142.
[23] M. Francis, J. Keesee, Airfoil dynamic stall performance with large-amplitude motions, AIAA Journal 23 (11) (1985) 1653–1659.